Lecture 2 : Microscopic Characterisation of Soils

Kenichi Soga, University of Cambridge

2-1 Engineering Properties of Granular Soils

The mechanical behavior of granular materials is governed primarily by their structure and the applied effective stresses. Structure depends on the arrangement of particles, density, and anisotropy. Particle sizes, shapes, and distributions, along with the arrangement of grains and grain contacts comprise the *soil fabric*.

Particle Shape

Particle shape is an inherent soil characteristic that plays a major role in mechanical behavior of soils. Characterization of particle shape is scale dependent, as shown in Fig. 2.1. At larger scales, that is, that of the particle itself, the particle *morphology* might be described as spherical, rounded, blocky, bulky, platy, elliptical, elongated, and so forth. At smaller scales, the *texture,* which reflects the local roughness features such as surface smoothness, roundness of edges and corners, and asperities is important.

With the exception of mica, most nonclay minerals in soils occur as bulky particles.[1] Most particles are not equidimensional, however, and are at least slightly elongate or tabular. A frequency histogram of particle length-to-width ratio (*L/W*) for Monterey No. 0 sand is shown in Fig. 2.2. This well-sorted beach sand is composed mainly of quartz with some feldspar. The mean of all the particle measurements is an *L/W* ratio of 1.39. This distribution is typical of that for many sands and silty sands.

Particle morphology in soil mechanics has historically been described using standard charts against which individual grains may be compared. A typical chart and some examples are shown in Fig. 2.3 (Krumbein, 1941; Krumbein and Sloss, 1963; Powers, 1953). *Sphericity* is defined as the ratio of the diameter of a sphere of equal volume to the particle to the diameter of the circumscribing sphere. *Roundness* is defined as the ratio of the average radius of curvature of the corners and edges of the particle to the radius of the maximum sphere that can be inscribed (Wadell, 1932). Sphericity and roundness are measures of two very different morphological properties.. Sphericity is most dependent on elongation, whereas roundness is largely dependent on the sharpness of angular protrusions from the particle. Different definitions of sphericity and roundness are available, as shown in Table 2.1. Due to the variety of definitions available, the quantification of particle shape requires accurate specification of their definition.

In recent years, techniques for computer analysis of shape data by digital imaging have improved greatly, and standard software applications include determination of aspect ratio and roundness. A convenient way to characterize particle shapes in more detail is by a Fourier mathematical technique. For instance, the *(R, θ)* Fourier method is in the following form:

$$R(\theta) = a_0 + \sum_{n=1}^{N} (a_n \cos n\theta + b_n \sin n\theta) \qquad (2.1)$$

[1] Quartz particles become flatter with decreasing size and may have a platy morphology when subdivided to a fineness approaching clay size (Krinsley and Smalley, 1973).

where $R(\theta)$ is the radius at angle θ, N is the total number of harmonics, n is the harmonic number, and a and b are coefficients giving the magnitude and phase for each harmonic. The lower harmonic numbers give the overall shape; for instance, the sphericity is expressed by the first and second harmonics. The coefficient values for higher-order descriptors generally decay with increasing descriptor or harmonic number, which expresses smaller features (i.e. texture) (Meloy, 1977). Other mathematical methods to curve-fit particle shapes are listed in Table 2.1. Further discussion on particle shape characterization is given by Barrett (1980), Hawkins (1993), Santamarina et al. (2001), and Bowman et al. (2001).

In an assembly of uniform size spherical particles, the loosest stable arrangement is the simple cubic packing giving a void ratio of 0.91. The densest packing is the tetrahedral arrangement giving a void ratio of 0.34. Particle shape affects minimum and maximum void ratios as shown in Fig. 2.4 (Youd, 1973). The values increase as particles become more angular or the roundness (defined as roundness 1 in Table 4.1) decreases. When $R = 1$, the particle is a sphere. As particles become more angular, R decreases to zero. Void ratios are also a function of particle size distribution; the values decrease as the range of particle sizes increases (increase in the coefficient of uniformity C_u).

The friction angle increases with increase in particle angularity, possibly as a result of an increase in coordination number. For example, values of the angle of repose[2] are plotted against roundness in Fig. 2.5 and the following linear fit to the relationship is proposed (Santamarina and Cho, 2004).

$$\phi'_{repose} = 42 - 17R \qquad (2.2)$$

where R is the coefficient of roundness defined as roundness 1 in Table 4.1. Similar data relating friction angle from drained triaxial tests and particle shape is presented by Sukumaran and Ashmawy (2001).

Particle Stiffness

Soil mass deformation at very small strains originates from the elastic deformations at points of contact between particles. Contact mechanics shows that the elastic properties of particles control the deformations at particle contacts (Johnson, 1985), and these deformations in turn influence the stiffness of particle assemblages. Elastic properties of different minerals and rocks are listed in Table 2.2. The modulus of a single grain, which determines the particle contact stiffness, is at least an order of magnitude greater than that of the particle assembly. Further details on the relation between particle stiffness and particle assemblage stiffness are given later in this Chapter.

Particle Strength

The crushability of soil particles has large effects on the mechanical behavior of granular materials. At high stresses, the compressibility of sand becomes large as a result of particle crushing, and the shape of an $e-log\ p$ compression curve becomes similar to that of normally

[2] Angle of repose can be determined by pouring soil in a graduated cylinder filled with water. Tilt the cylinder more than 60° and bring it back slowly to the vertical position. The angle of the residual sand slope is the angle of repose. Further details of the method can be found in Santamarina and Cho (2004).

consolidated clay (Miura et al. 1984; Coop, 1990; Yasufuku et al., 1991). Under constant states of stress, the amount of particle breakage increases with time, contributing to creep of the soil (Lade et al., 1996). The amount of crushing in a soil mass depends both on the stiffness and strength of the individual grains and how applied stresses are transmitted through the assemblage of soil particles.

Particle strength or hardness is characterized by crushing at contacts or particle tensile splitting. There is a statistical variation in grain strength for particles of a specified material and of a given size (Moroto and Ishii, 1990; McDowell, 2001). Random variation in grain strengths leads to distributions of particle sizes when large stress is applied to a soil assembly. Table 2.3 lists the characteristic tensile strengths of some soil particles. The values are smaller than the yield strength of the material itself. The strength also depends on the particle shape. For example, Hagerty et al. (1993) show that angular glass beads were more susceptible to breakage than round glass beads.

The breakage potential of a single soil particle increases with its size as illustrated in Table 2.3. This is because larger particles tend to contain more and larger internal flaws and hence have lower tensile strength. Fig. 2.6 shows that oolitic limestone, carboniferous limestone, and quartz sand exhibit near linear declines in strength with increasing particle size on a log−log plot (Lee, 1992).

The amount of particle crushing in an assemblage of particles depends not only on particle strength, but also on the distribution of contact forces and arrangement of different size particles. It can be argued that larger size particles are more likely to break because the normal contact forces in a soil element increase with particle size and the probability of a defect in a given particle increases with its size as shown in Fig 2.6 (Hardin, 1985). However, if a larger particle has contacts with neighboring particles (i.e., larger coordination number), the load on it is distributed, and the probability of facture is less than for a condition with fewer contacts. Experimental evidences suggest that fines increase as particles break by increase in applied pressure. For example, the evolution of particle size distribution curves for Ottawa sand in one-dimensional compression is shown in Fig. 2.7 (Hagerty et al., 1993). Hence, the coordination number dominates over size-dependent particle strength. Larger particles have higher coordination numbers because they are in contact with many smaller particles. The very smallest particles have a lower coordination number because there are fewer smaller particles available for contact. Hence, the largest particles in the aggregate become protected by the surrounding newly formed smaller particles, and smaller particles are more likely to break or move.

2-2 Frictional Behaviour of Minerals

Evaluation of the true coefficient of friction μ and friction angle ϕ_μ is difficult because it is very difficult to do tests on two very small particles that are sliding relative to each other, and test results for particle assemblages are influenced by particle rearrangements, volume changes, surface preparation factors, etc. Some values are available, however, and they are presented and discussed in this section.

Values of the true friction angle ϕ_μ for several minerals are listed in Table 2.4, along with the type of test and conditions used for their determination. A pronounced antilubricating effect of water is evident for polished surfaces of the bulky minerals quartz, feldspar, and

calcite. This apparently results from a disruptive effect of water on adsorbed films that may have acted as a lubricant for dry surfaces. Evidence for this is shown in Fig. 2.8, where it may be seen that the presence of water had no effect on the frictional resistance of quartz surfaces that had been chemically cleaned prior to the measurement of the friction coefficient. The samples tested by Horn and Deere (1962) in Table 2.4 had not been chemically cleaned.

An apparent antilubrication effect by water might also arise from attack of the silica surface (quartz and feldspar) or carbonate surface (calcite) and the formation of silica and carbonate cement at interparticle contacts. Many sand deposits exhibit "aging" effects wherein their strength and stiffness increase noticeably within periods of weeks to months after deposition, disturbance, or densification, as described, for example, by Mitchell and Solymar (1984), Mitchell (1986), Mesri et al. (1990), and Schmertmann (1991). Increases in penetration resistance of up to 100 percent have been measured in some cases. The relative importance of chemical factors, such as precipitation at interparticle contacts, changes in surface characteristics, and mechanical factors, such as time-dependent stress redistribution and particle reorientations, in causing the observed behavior is not known.

As surface roughness increases, the apparent antilubricating effect of water decreases. This is shown in Fig. 2.8 for quartz surfaces that had not been cleaned. Chemically cleaned quartz surfaces, which give the same value of friction when both dry and wet, show a loss in frictional resistance with increasing surface roughness. Evidently, increased roughness makes it easier for asperities to break through surface films. The decrease in friction with increased roughness is not readily explainable. One possibility is that the cleaning process was not effective on the rough surfaces.

For soils in nature, the surfaces of bulky mineral particles are most probably rough relative to the scale in Fig. 2.8, and they will not be chemically clean. Thus, values of $\mu = 0.5$ and $\phi_\mu = 26°$ are reasonable for quartz, both wet and dry.

On the other hand, water apparently acts as a lubricant in sheet minerals, as shown by the values for muscovite, phlogopite, biotite, and chlorite in Table 2.4. This is because in air the adsorbed film is thin, and surface ions are not fully hydrated. Thus, the adsorbed layer is not easily disrupted. Observations have shown that the surfaces of the sheet minerals are scratched when tested in air (Horn and Deere, 1962). When the surfaces of the layer silicates are wetted, the mobility of the surface films is increased because of their increased thickness and because of greater surface ion hydration and dissociation. Thus, the values of ϕ_μ listed in Table 2.4 for the sheet minerals under saturated conditions (7°−13°) are probably appropriate for sheet mineral particles in soils.

2-3 Physical Interactions among particles

Continuum mechanics assumes that applied forces are transmitted uniformly through a homogenized granular system. In reality, however, the interparticle force distributions are strongly inhomogeneous, and the applied load is transferred through a network of interparticle force chains. The generic disorder of particles, local spatial fluctuations of coordination number, and positions of neighboring particles produce packing constraints and disorder. This geometric disorder of particles leads to inhomogeneous but structured force distributions within the granular system. Deformation is associated with buckling of these force chains, and energy is dissipated by sliding at the clusters of particles between the force chains.

Discrete particle numerical simulations, such as the discrete (distinct) element method (Cundall and Strack, 1979) and the contact dynamics method (Moreau, 1994), offer physical insights into particle interactions and load transfers that are difficult to deduce from physical experiments. Typical inputs for the simulations are particle packing conditions and interparticle contact characteristics such as the interparticle friction angle ϕ_μ. Complete details of these numerical methods are beyond the scope of this book; additional information can be found in Oda and Iwashita (1999). However, some of the main findings are useful for developing an improved understanding of how stresses are carried through discrete particle systems such as soils and how these distributions influence the deformation and strength properties.

Strong Force Networks and Weak Clusters

Examples of the computed normal contact force distribution in a granular system are shown in Figs. 2-9a for an isotropically loaded condition and 2-9b for a biaxial loaded condition (Thornton and Barnes, 1986). The thickness of the lines in the figure is proportional to the magnitude of the contact force. The external loads are transmitted through a network of interparticle contact forces represented by thicker lines. This is called the *strong force network* and is the key microscopic feature of load transfer through the granular system. The scale of statistical homogeneity in a two-dimensional particle assembly is found to be a few tens of particle diameters (Radjai et al., 1996). Forces averaged over this distance could therefore be expected to give a stress that is representative of the macroscopic stress state. The particles not forming a part of the strong force network are floating like a fluid with small loads at the interparticle contacts. This can be called the *weak cluster*, which has a width of 3 to 10 particle diameters.

Both normal and tangential forces exist at interparticle contacts. Figure 2.10 shows the probability distributions (P_N and P_T) of normal contact forces N and tangential contact forces T for a given biaxial loading condition. The horizontal axis is the forces normalized by their mean force value ($<N>$ or $<T>$), which depend on particle size distribution (Radjai et al., 1996). The individual normal contact forces can be as great as six times the mean normal contact force, but approximately 60 percent of contacts carry normal contact forces below the mean (i.e., weak cluster particles). When normal contact forces are larger than their mean, the distribution law of forces can be approximated by an exponentially decreasing function; Radjai et al. (1996) show that $P_N(\xi = N/<N>) = k\mathrm{e}^{1.4(1-\xi)}$ fits the computed data well for both two- and three-dimensional simulations. The exponent was found to change very slightly with the coefficient of interparticle friction and to be independent of particle size distributions.

Simulations show that deviator load is transferred exclusively by the normal contact forces in the strong networks, and the contribution by the weak clusters is negligible. This is illustrated in Fig. 2.11, which shows the normal contact forces contribute greater than the tangential contact forces to the development of the deviator stress during axisymmetric compression of a dense granular assembly (Thornton, 2000). The strong force network carries most of the whole deviator load as shown in Fig. 2.12 and is the load-bearing part of the structure. For particles in the strong networks, the tangential contact forces are much smaller than the interparticle frictional resistance because of the large normal contact forces. In contrast, the numerical analysis results show that the tangential contact forces in the weak clusters are close to the interparticle frictional resistance. Hence, the frictional resistance is almost fully mobilized between particles in the weak clusters, and the particles are behaving like a viscous fluid.

Buckling, Sliding, and Rolling

As particles begin to move relative to each other during shear, particles in the strong force network do not slide, but columns of particles buckle (Cundall and Strack, 1979). Particles in the strong force network collapse upon buckling, and new force chains are formed. Hence, the spatial distributions of the strong force network are neither static nor persistent features.

At a given time of biaxial compression loading, particle sliding is occurring at almost 10 percent of the contacts (Kuhn, 1999) and approximately 96 percent of the sliding particles are in the weak clusters (Radjai et al., 1996). Over 90 percent of the energy dissipation occurs at just a small percentage of the contacts (Kuhn, 1999). This small number of sliding particles is associated with the ability of particles to roll rather than to slide. Particle rotations reduce contact sliding and dissipation rate in the granular system. If all particles could roll upon one another, a granular assembly would deform without energy dissipation.[3] However, this is not possible owing to restrictions on particle rotations. It is impossible for all particles to move by rotation, and sliding at some contacts is inevitable due to the random position of particles (Radjai and Roux, 1995).[4] Some frictional energy dissipation can therefore be considered a consequence of disorder of particle positions.

As deformation progresses, the number of particles in the strong force network decreases, with fewer particles sharing the increased loads (Kuhn, 1999). Figure 2.13 shows the spatial distribution of residual deformation, in which the computed deformation of each particle is subtracted from the average overall deformation (Williams and Rege, 1997). A group of interlocked particles that instantaneously moves as a rigid body in a circular manner can be observed. The outer boundary of the group shows large residual deformation, whereas the center shows very small residual deformation. The rotating group of interlocked particles, which can be considered as a weak cluster, becomes more apparent as applied strains increase toward failure. The bands of large residual deformation [termed *microbands* by Kuhn (1999)] are where particle translations and rotations are intense as part of the strong force network. Kuhn (1999) reports that their thicknesses are $1.5D_{50}$ to $2.5D_{50}$ in the early stages of shearing and increase to between $1.5D_{50}$ and $4D_{50}$ as deformation proceeds. This microband slip zone may eventually become a localized shear band.

Fabric Anisotropy

The ability of a granular assemblage of particles to carry deviatoric loads is attributed to its capability to develop anisotropy in contact orientations. An initial isotropic packing of particles develops an anisotropic contact network during compression loading. This is because new contacts form in the direction of compression loading and contacts that orient along the direction perpendicular to loading direction are lost.

The initial state of contact anisotropy (or fabric) plays an important role in the subsequent deformation. Figure 2.14 shows results of discrete particle simulations of particle assemblies prepared at different states of initial contact anisotropy under an isotropic stress condition (Yimsiri, 2001). The initial void ratios are similar ($e_0 \approx 0.75$ to 0.76) and both drained triaxial

---

[3] This assumes that the particles are rigid and rolling with a single point contact. In reality, particles deform and exhibit rolling resistance. Iwashita and Oda (1998) state that the incorporation of rolling resistance is necessary to generate realistic localized shear bands.

[4] For instance, consider a chain loop of an odd number of particles. Particle rotation will involve at least one sliding contact.

compression and extension tests were simulated. Although all specimens are initially isotropically loaded, the directional distributions of contact forces are different due to different orientations of contact plane normals (sample A: more in the vertical direction; sample B: similar in all directions; sample C: more in the horizontal direction). As shown in Fig. 2.14*a*, both samples A and C showed stiffer response when the compression loading was applied in the preferred direction of contact forces, but softer response when the loading was perpendicular to the preferred direction of contact forces. The response of sample B, which had an isotropic fabric, was in between the two. Dilation was most intensive when the contact forces were oriented preferentially in the direction of applied compression; and experimental data presented by Konishi et al. (1982) shows a similar trend.

Figure 2.14*b* shows the development of fabric anisotropy with increasing strain. The degree of fabric anisotropy is expressed by a fabric anisotropy parameter A; the value of A increases with more vertically oriented contact plane normals and is negative when there are more horizontally oriented contact plane normals.[5] The fabric parameter gradually changes with increasing strains and reaches a steady state value as the specimens fail. The final steady state value is independent of the initial fabric, indicating that the inherent anisotropy is destroyed by the shearing process. The final fabric anisotropy after triaxial extension is larger than that after triaxial compression because the additional confinement by a larger intermediate stress in the extension tests created a higher degree of fabric anisotropy.

Close examination of the contact force distribution for the strong force network and weak clusters gives interesting microscopic features. Figure 2.15 shows the values of A determined for the subgroups of contact forces categorized by their magnitudes when the specimen is under a biaxial compression loading condition (Radjai, 1999). The direction of contact anisotropy of the weak clusters ($N/\langle N\rangle$ less than 1) is orthogonal to the direction of compression loading, whereas that of the strong force network ($N/\langle N\rangle$ more than 2) is parallel. Figure 2.16 shows the evolution of fabric with strains in biaxial loading (Thornton and Antony, 1998). The fabric anisotropy is separated into that in the strong force networks ($N/\langle N\rangle$ of more than 1) and that in the weak clusters ($N/\langle N\rangle$ less than 1). Again the directional evolution of the fabric in the weak clusters is opposite to the direction of loading. Therefore, the stability of the strong force chains aligned in the vertical loading direction is obtained by the lateral forces in the surrounding weak clusters.

Changes in Number of Contacts and Microscopic Voids

At the beginning of biaxial loading of a dense granular assembly, more contacts are created from the increase in the hydrostatic stress, and the local voids become smaller. As the axial stress increases, however, the local voids tend to elongate in the direction of loading as shown in Fig. 2.17. Consequently particle contacts are lost. As loading progresses, vertically elongated local voids become more apparent, leading to dilation in terms of overall sample volume (Iwashita and Oda, 2000).

---

[5] The density of contact plane normals $E(\theta)$ with direction θ is fitted with the following expression (Radjai, 1999):

$$E(\theta) = \frac{c}{\pi}\{1 + A\cos 2(\theta - \theta_c)\}$$

where c is the total number of contacts, θ_c is the direction for which the maximum E is reached, and the magnitude of A indicates the amplitude of anisotropy. When the directional distribution of contact forces is independent of θ, the system has an isotropic fabric and $A = 0$.

Void reduction is associated with particle breakage. Thus, there is a need to incorporate grain crushing in discrete particle simulations to model the contractive behavior of soils (Cheng et al., 2003). Normal contact forces in the strong force network are quire high, and, therefore, particle asperities, and even particles themselves, are likely to break, causing the force chains to collapse.

Local voids tend to change size even after the applied stress reaches the failure stress state (Kuhn, 1999). This suggests that the degrees of shearing required for the stresses and void ratio to reach the critical state are different. Numerical simulations by Thornton (2000) show that at least 50 percent axial strain is required to reach the critical state void ratio.

Macroscopic Friction Angle Versus Interparticle Friction Angle

Discrete particle simulations show that an increase in the interparticle friction angle ϕ_μ results in an increase in shear modulus and shear strength, in higher rates of dilation, and in greater fabric anisotropy. Figure 2.18 shows the effect of assumed interparticle friction angle ϕ_μ on the mobilized macroscopic friction angle of the particle assembly (Thornton, 2000; Yimsiri, 2001). The macroscopic friction angle is larger than the interparticle friction angle if the interparticle friction angle is smaller than 20°. As the interparticle friction becomes more than 20°, the contribution of increasing interparticle friction to the macroscopic friction angle becomes relatively small; the macroscopic friction angle ranges between 30° and 40° when the interparticle friction angle increases from 30° to 90°.[6]

The nonproportional relationship between macroscopic friction angle of the particle assembly and interparticle friction angle results because deviatoric load is carried by the strong force networks of normal forces and not by tangential forces, whose magnitude is governed by interparticle friction angle. Increase in interparticle friction results in a decrease in the percentage of sliding contacts (Thornton, 2000). The interparticle friction therefore acts as a kinematic constraint of the strong force network and not as the direct source of macroscopic resistance to shear. If the interparticle friction were zero, strong force chains could not develop, and the particle assembly will behave like a fluid. Increased friction at the contacts increases the stability of the system and reduces the number of contacts required to achieve a stable condition. As long as the strong force network can be formed, however, the magnitude of the interparticle friction becomes of secondary importance.

The above findings from discrete particle simulations are partially supported by the experimental data given by Skinner (1969), which are also shown in Fig. 2.18. He performed shear box tests on spherical particles with different coefficients of interparticle friction angle. The tested materials included glass ballotini, steel ball bearings, and lead shot. Use of glass ballotini was particularly attractive since the coefficient of interparticle friction increases by a factor of between 3.5 and 30 merely by flooding the dry sample. Skinner's data shown in Fig. 2.18 indicate that the macroscopic friction angle is nearly independent of interparticle friction angle.

Effects of Particle Shape and Angularity

A lower porosity and a larger coordination number are achieved for ellipsoidal particles compared to spherical particles (Lin and Ng, 1997). Hence, a denser packing can be achieved

---

[6] Reference to Table 2.4 shows that actually measured values of ϕ_μ for geomaterials are all less than 45º. Thus, numerical simulations done assuming larger values of ϕ_μ appear to give unrealistic results.

for ellipsoidal particles. Ellipsoid particles rotate less than spherical particles. An assembly of ellipsoid particles gives larger values of shear strength and initial modulus than an assemblage of spherical particles, primarily because of the larger coordination number for ellipsoidal particles. Similar findings result for two dimensional particle assemblies. Circular disks give the highest dilation for a given stress ratio and the lowest coordination number compared to elliptical or diamond shapes (Williams and Rege, 1997). An assembly of rounded particles exhibits greater softening behavior with fabric anisotropy change with strain, whereas an assembly of elongated particles requires more shearing to modify its initial fabric anisotropy to the critical state condition (Nouguier-Lehon et al., 2003).

Table 2.1 Methods for Particle Shape Characterization

Method	Definition
Morphology−Sphere	
Sphericity 1	$\dfrac{\text{Diameter of a sphere of equal volume}}{\text{Diameter of circumscribing sphere}}$
Sphericity 2	$\dfrac{\text{Particle volume}}{\text{Volume of circumscribing sphere}}$
Sphericity 3	
Projection sphericity	$\dfrac{\text{Area of particle outline}}{\text{Area of a circle with diameter equal to the longest length of outline}}$
Inscribed circle sphericity	$\dfrac{\text{Diameter of the largest inscribed circle}}{\text{Diameter of the smallese inscribed circle}}$
Morphology−Ellipse	
Eccentricity	δ_p/R_{ap}, where the ellipse is characterized by $R_p+\delta_p cos2\theta$ in polar coordinates
Elongation	$\dfrac{\text{Smallest diameter}}{\text{Diameter perpendicular to the smallest diameter}}$
Slenderness	$\dfrac{\text{Maximum dimension}}{\text{Minimum dimension}}$
Texture−Roundness	
Roundness 1	$\dfrac{\text{Average of radius of curveture of surface features, } \left(\sum r_i\right)/N}{\text{Radius of the maximum sphere that can be inscribed, } r_{\max}}$
Roundness 2	$\dfrac{\text{Radius of curveture of the most convex part}}{0.5\text{ (longest diameter through the most convex part)}}$
Roundness 3	$\dfrac{\text{Radius of curveture of the most convex part}}{\text{Mean radius}}$
Morphology/Texture	
Fourier method	Eq. (4.3), first and second harmonics characterize sphericity, whereas higher harmonics (around 10^{th}) characterize roundness. Surface texture is characterized by much higher harmonics.
Fourier descriptor method	More flexible that the Fourier method by using the complex plane (Bowman et al., 2001). Lower harmonics give shape characteristics such as elongation, triangularity, squareness, and asymmetry. Higher harmonics (larger than 8^{th}) give textural features.
Fractal analysis	Use as a measure of texture (Vallejo, 1995; Santamarina et al. 2001).

From Hawkins (1993), Santamarina et al. (2001), and Bowman et al. (2001).

Table 2.2 Elastic Properties of Geomaterials at Room Temperature

Material	Young's Modulus (GPa)	Shear Modulus (GPa)	Poisson's Ratio
Quartz	76	29	0.31
Limestone	2 – 97	1.6 – 38	0.01 – 0.32
Basalt	25 – 183	3 – 27	0.09 – 0.35
Granite	10 – 86	7 – 70	0.00 – 0.30
Hematite	67 – 200	27 – 78	—
Magnetite	31	19	—
Shale	0.4 – 68	5 – 30	0.01 – 0.34

After Santamarina et al., (2001).

Table 2.3 Strength of Soil Particles

Sand Name	Size (mm)	37% Tensile Strength (MPa)	Mean Strength (MPa)	Reference
Quartz				
Leighton Buzzard silica sand	1.18	−	29.8	Lee (1992)
	2.0	−	24.7	
	3.36	−	20.5	
Toyoura sand	0.2	147.4	136.6	Nakata et al. (2001)
Aio quartz sand	0.85	51.2	52.1	Nakata et al. (1999)
	1.0	47.7	46.6	
	1.18	37.9	35.6	
	1.4	46.7	42.4	
	1.7	39.6	38.5	
Silica sand	0.5	147.4	132.5	McDowell (2001)
	1	66.7	59.0	
	2	41.7	37.3	
Silica sand	0.28	110.9	147.3	Nakata et al. (2001)
	0.66	72.9	73.1	
	1.55	31.0	29.7	
Feldspar				
Aio feldspar sand	0.85	20.9	24.6	Nakata et al. (1999)
	1.0	24.3	22.8	
	1.18	18.1	18.2	
	1.4	23.1	21.4	
	1.7	18.9	18.3	
Calcareous Sand				
Oolitic limestone particle	5	−	2.4	Lee (1992)
	8	−	2.1	
	12	−	1.8	
	20	−	1.5	
	30	−	1.3	
	40	−	1.2	
	50	−	1.1	
Carboniferous limestone particle	5	−	14.9	
	8	−	12.2	Lee (1992)
	12	−	10.3	
	20	−	8.3	
	30	−	7.0	
	40	−	6.2	
	50	−	5.7	
Quiou sand	1	109.3	96.19	McDowell and Amon (2000)
	2	41.4	36.20	
	4	4.2	3.87	
	8	0.73	0.63	
	16	0.6	0.54	
Others				
Masado decomposed granite soil	1.55	24.2	22.1	Nakata et al. (2001)
Glass beads	0.93	365.8	339.6	Nakata et al. (2001)
Angular glass	0.93	62.1	60.0	Nakata et al. (2001)

Table 2.4 Values of Friction Angle (ϕ_μ) Between Mineral Surfaces.

Mineral	Type of Test	Conditions	ϕ_μ (deg)	Comments	Reference
Quartz	Block over particle set in mortar	Dry	6	Dried over $CaCl_2$ before testing	Tschebotarioff and Welch (1948)
		Moist	24.5		
		Water saturated	24.5		
Quartz	Three fixed particles over block	Water saturated	21.7	Normal load per particle increasing from 1 g to 100 g	Hafiz (1950)
Quartz	Block on block	Dry	7.4	Polished surfaces	Horn and Deere (1962)
		Water saturated	24.2		
Quartz	Particles on polished block	Water saturated	22–31	ϕ decreasing with increasing particle size	Rowe (1962)
Quartz	Block on block	Variable	0–45	Depends on roughness and cleanliness	Bromwell (1966)
Quartz	Particle–particle	Saturated	26	Single-point contact	Procter and Barton (1974)
	Particle–plane	Saturated	22.2		
	Particle–plane	Dry	17.4		
Feldspar	Block on block	Dry	6.8	Polished surfaces	Horn and Deere (1962)
		Water saturated	37.6		
Feldspar	Free particles on flat surface	Water saturated	37	25–500 sieve	Lee (1966)
Feldspar	Particle–plane	Saturated	28.9	Single-point contact	Procter and Barton (1974)
Calcite	Block on block	Dry	8.0	Polished surfaces	Horn and Deere (1962)
		Water saturated	34.2		
Muscovite	Along cleavage faces	Dry	23.3	Oven dry	Horn and Deere (1962)
		Dry	16.7	Air equilibrated	
		Saturated	13.0		
Phlogopite	Along cleavage faces	Dry	17.2	Oven dry	Horn and Deere (1962)
		Dry	14.0	Air equilibrated	
		Saturated	8.5		
Biotite	Along cleavage faces	Dry	17.2	Oven dry	Horn and Deere (1962)
		Dry	14.6	Air equilibrated	
		Saturated	7.4		
Chlorite	Along cleavage faces	Dry	27.9	Oven dry	Horn and Deere (1962)
		Dry	19.3	Air equilibrated	
		Saturated	12.4		

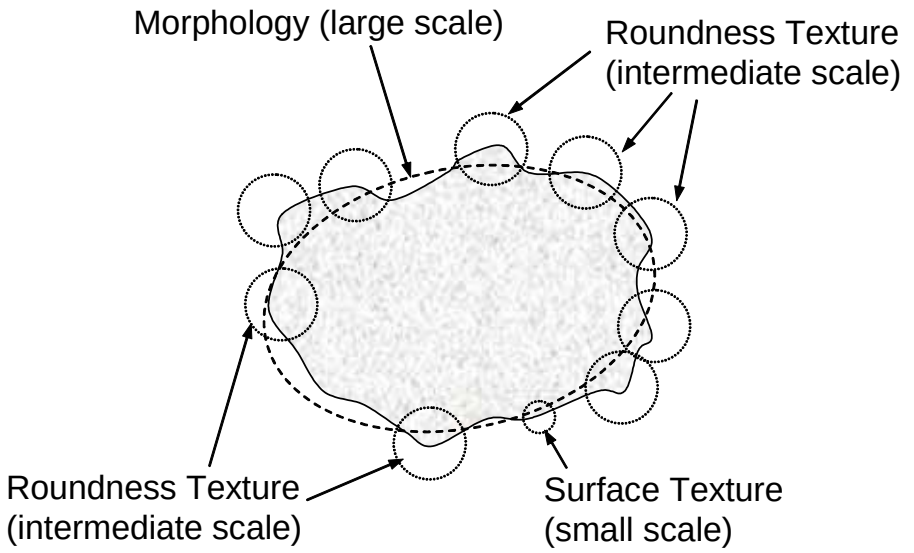

Fig. 2-1

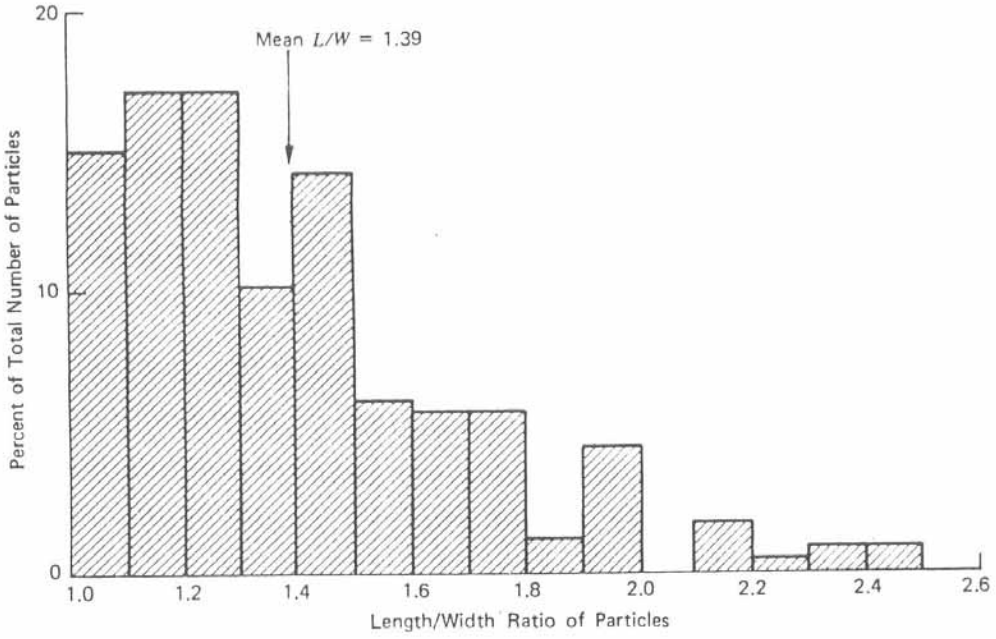

Fig. 2-2

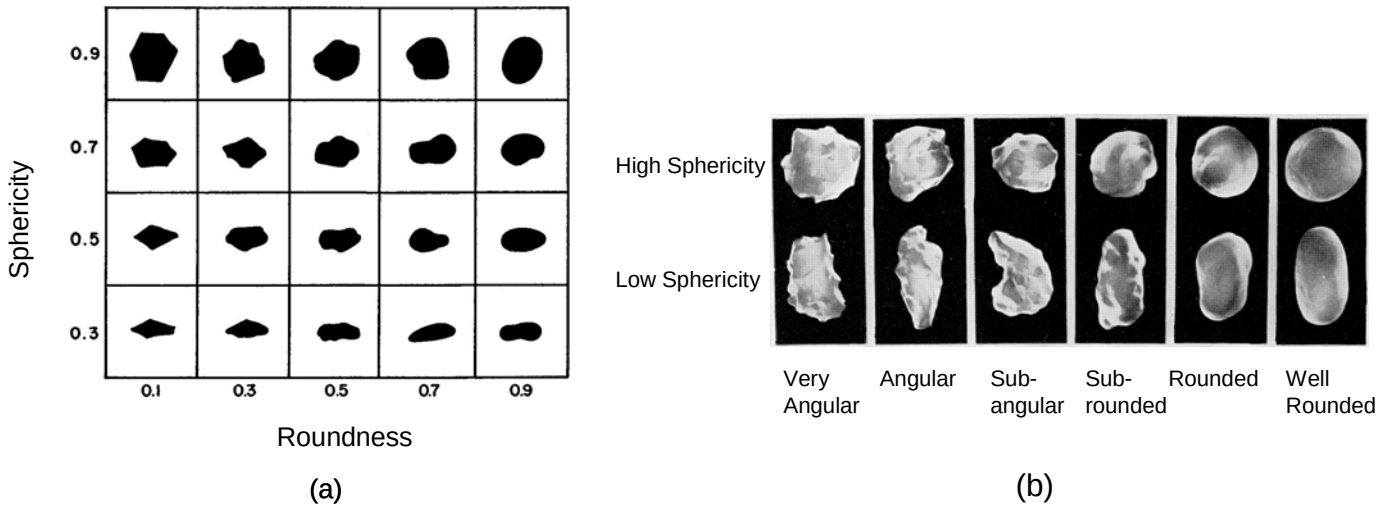

Fig. 2-3

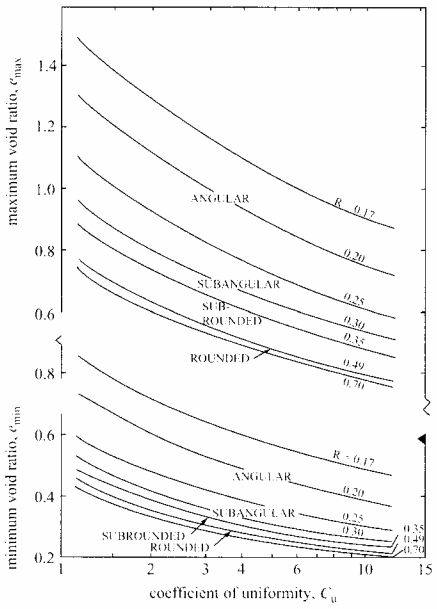

Fig. 2-4

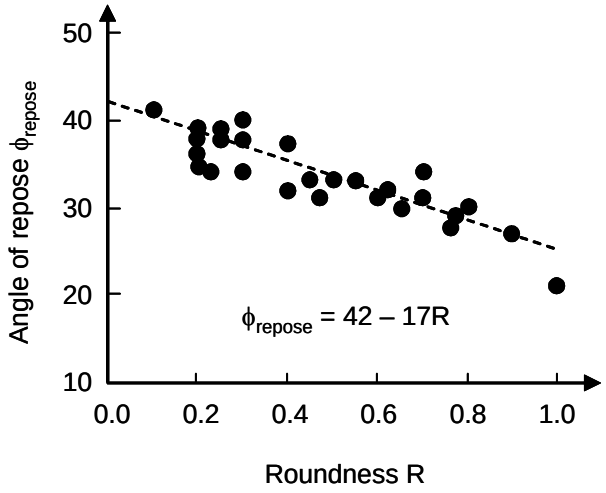

Fig. 2-5

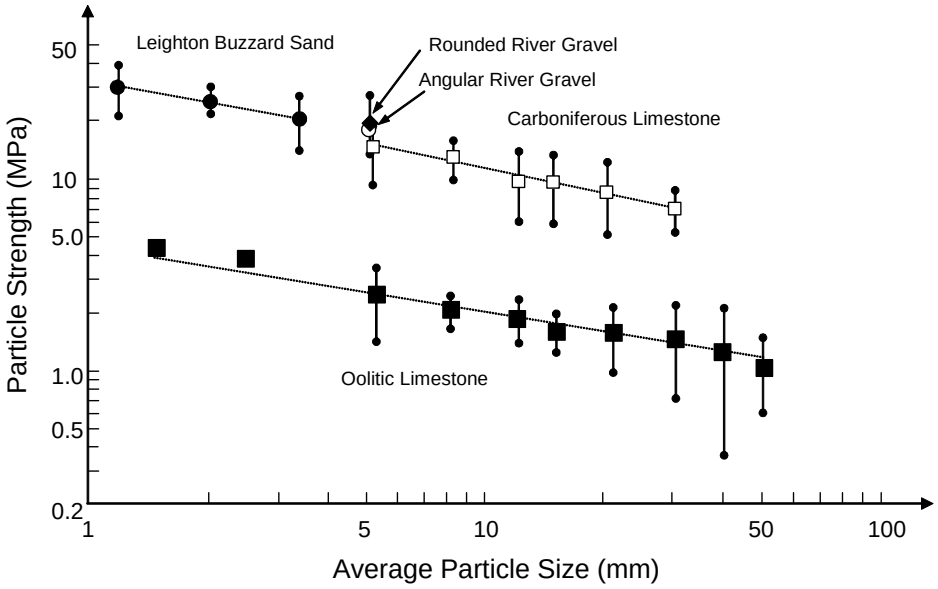

Fig. 2-6

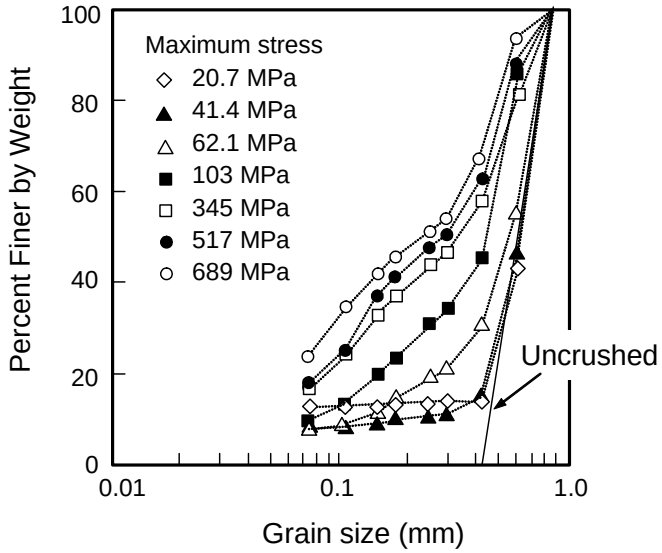

Fig. 2-7

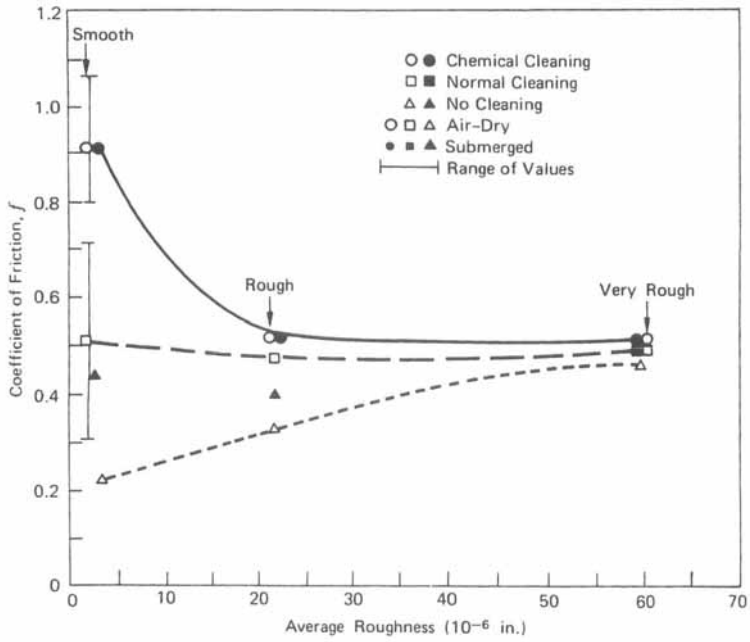

Fig. 2-8

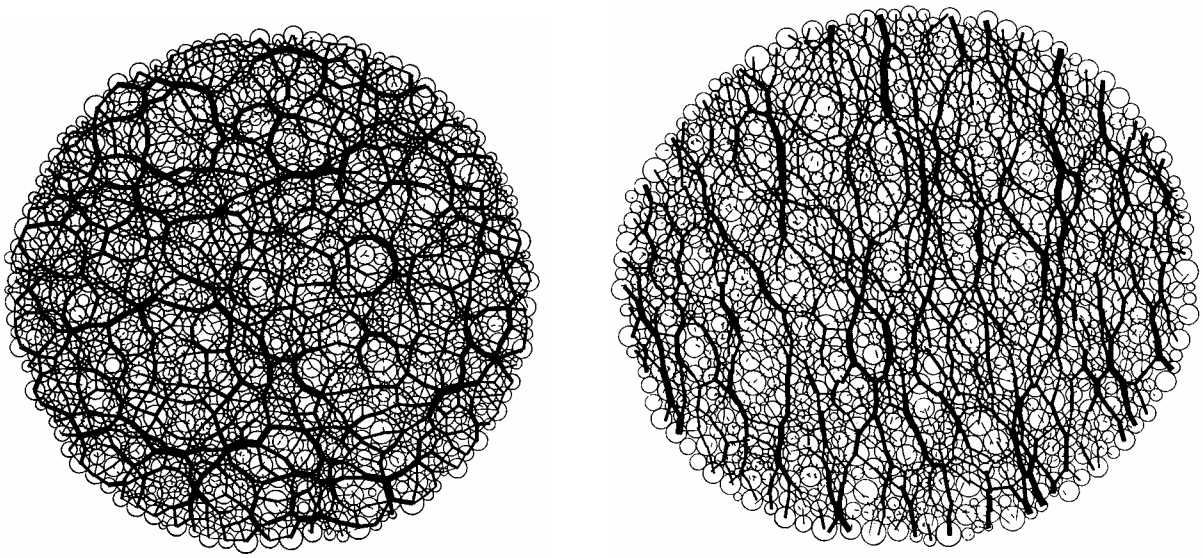

(a) (b)

Fig. 2-9

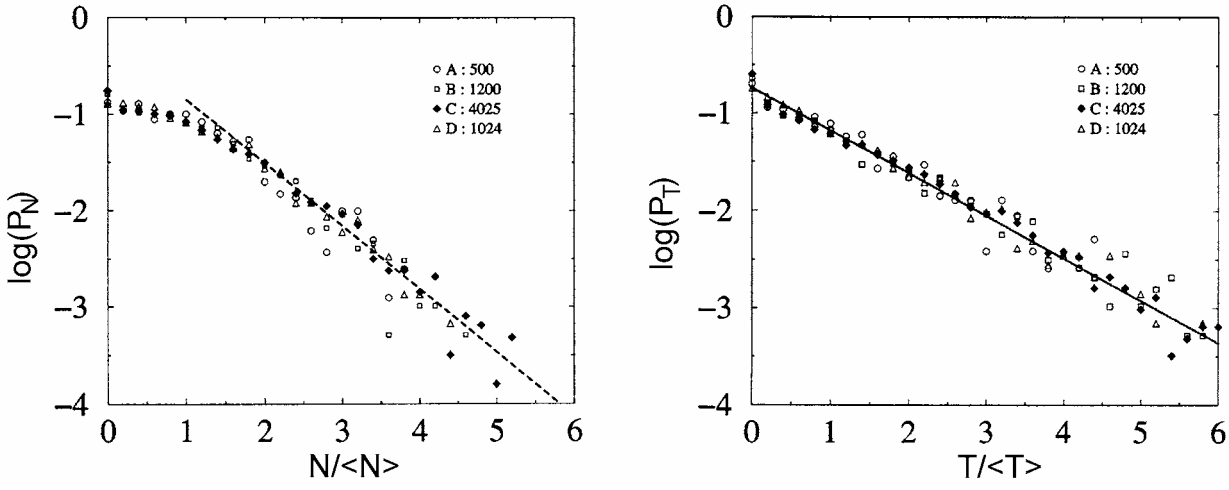

(a) (b)

Fig. 2-10

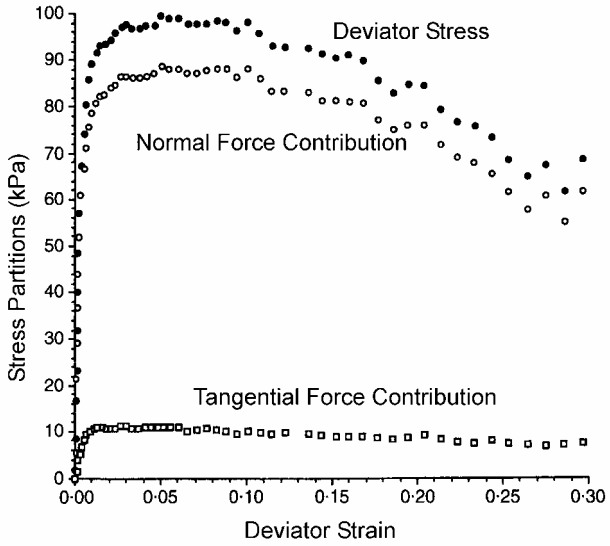

Fig. 2-11

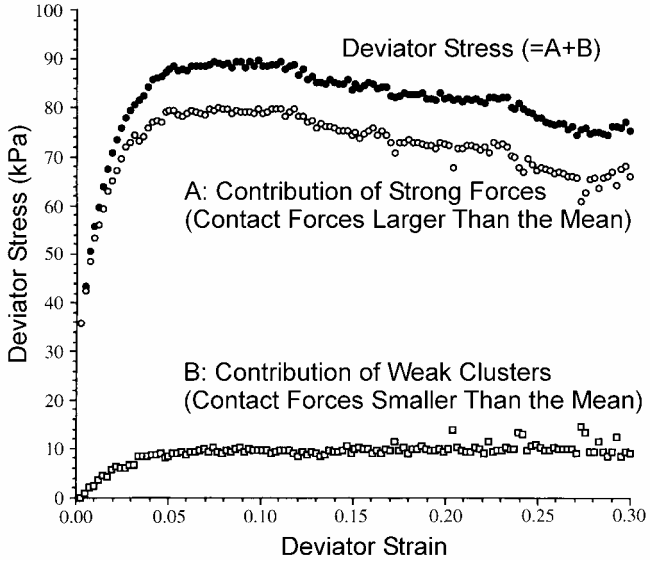

Fig. 2-12

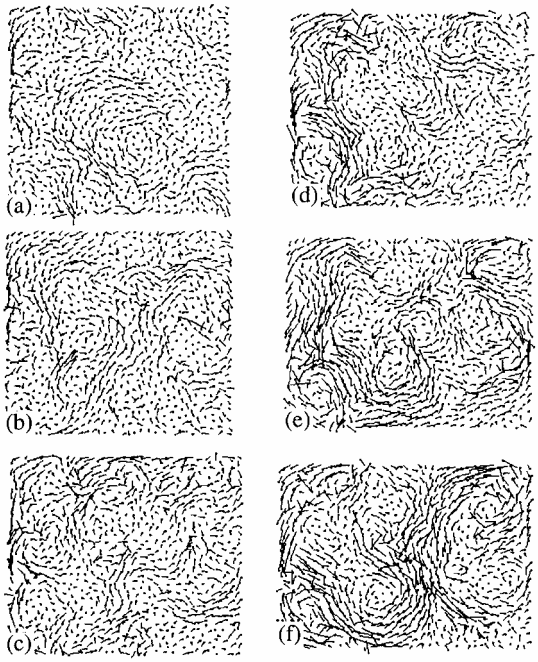

Fig. 2-13

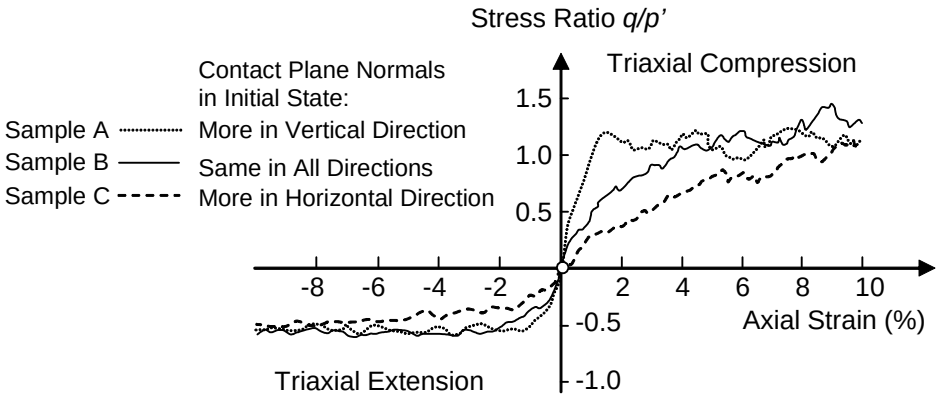

(*a*)

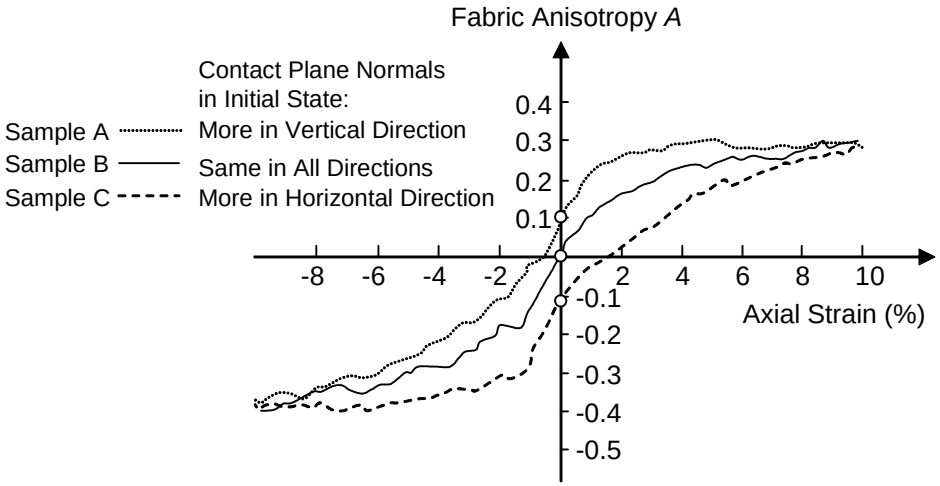

(*b*)

Fig. 2-14

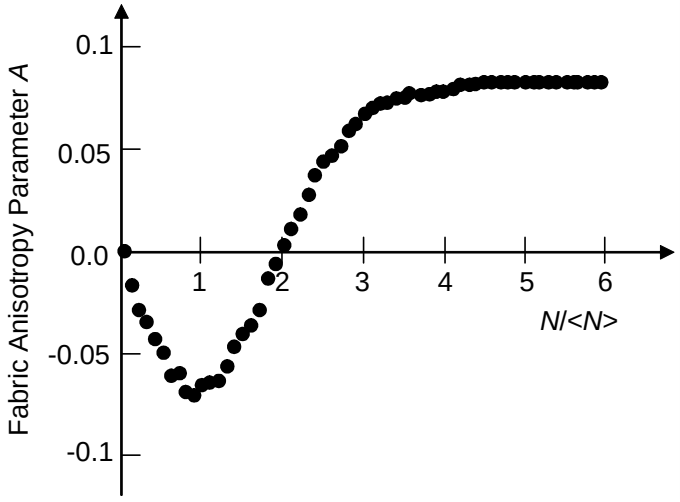

Fig. 2-15

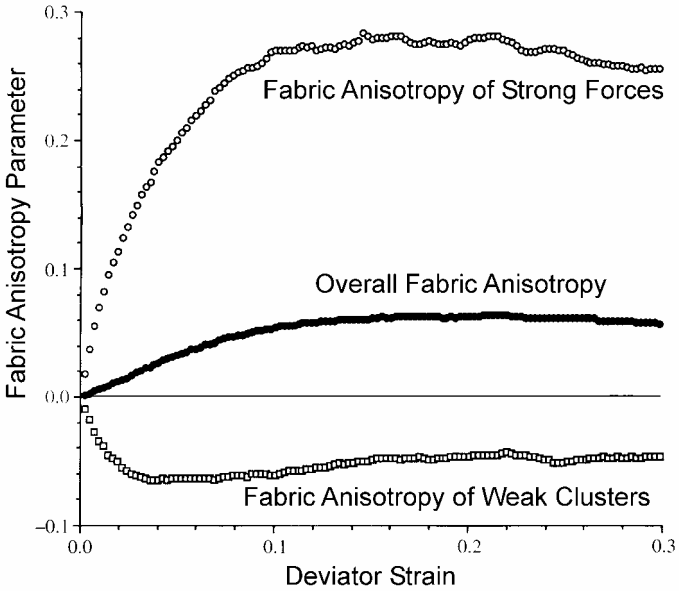

Fig. 2-16

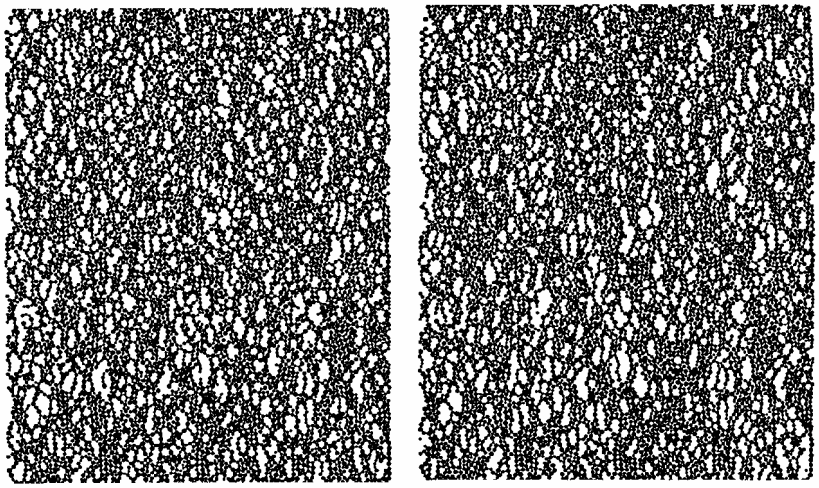

(a) Axial strain 1.1%　　(b) Axial strain 2.2%

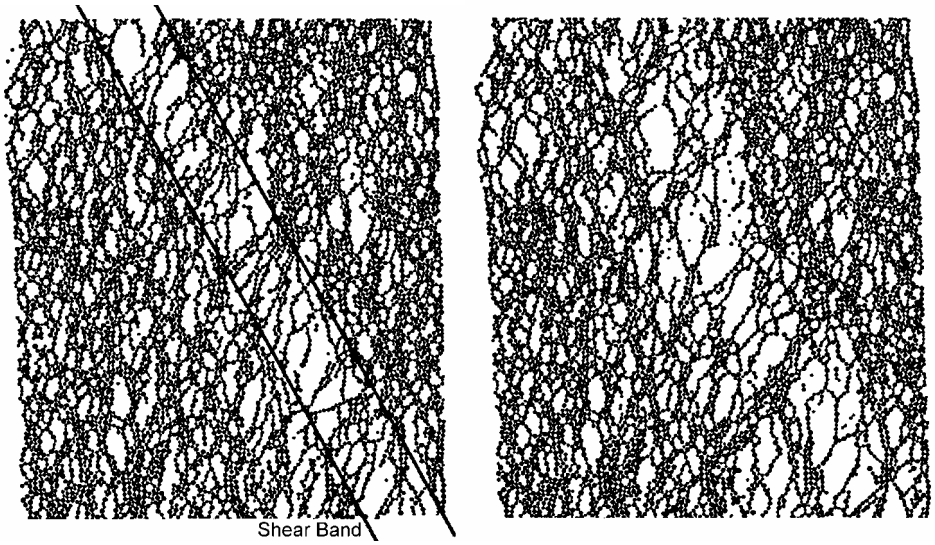

(c) Axial strain 4.4%　　(d) Axial strain 5.5%

Fig. 2-17

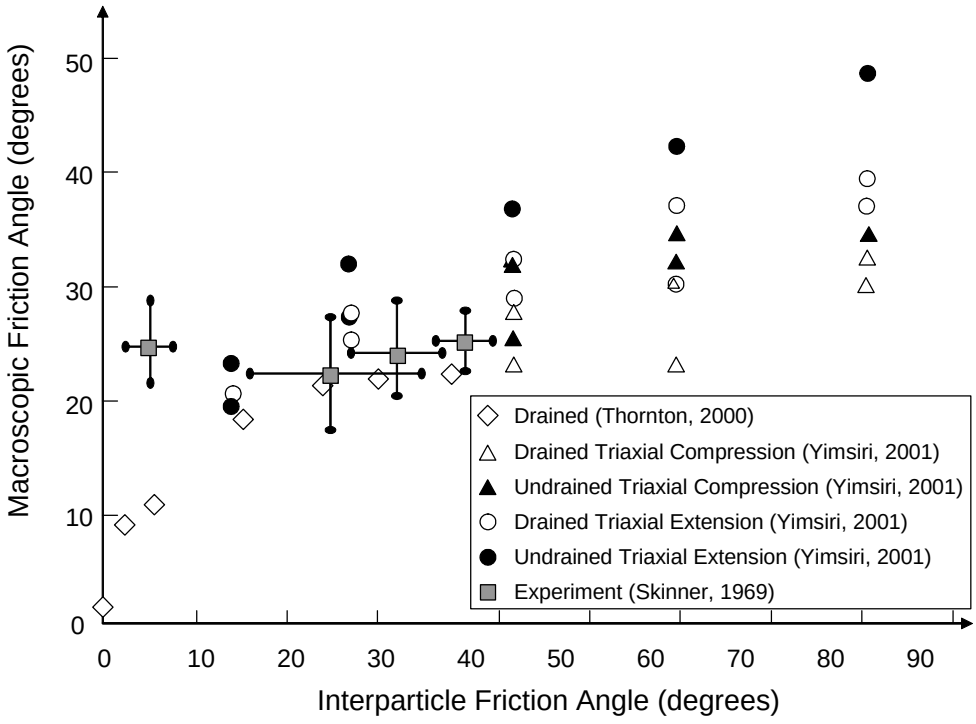

Fig. 2-18